Power Electronic Systems
Laboratory

IEEE Transactions on Industrial Electronics, Vol. 67, No. 10, pp. 8817-8828, October 2020

Experimental Analysis and Optimization of a Contactless Eddy-Current-Based Speed Sensor for Smooth Conductive Surfaces

C. Gong,
A. Tüysüz,
M. Flankl,
T. Stolz,
J. W. Kolar,
T. Habetler

Eidgenössische Technische Hochschule Zürich
Swiss Federal Institute of Technology Zurich

Experimental Analysis and Optimization of a Contactless Eddy-Current-Based Speed Sensor for Smooth Conductive Surfaces

Cheng Gong[1,2], Arda Tüysüz[1], Michael Flankl[1], Tibor Stolz[1], Johann W. Kolar[1] and Thomas Habetler[2]
[1]Power Electronic Systems Laboratory, ETH Zurich, Zurich, 8092 Switzerland
[2]School of Electrical and Computer Engineering, Georgia Institute of Technology, Atlanta, GA, 30318 USA

***Abstract*—Speed sensing is an essential part in all closed-loop systems. There exist some situations in industry where the speed has to be measured without touching the target object, for example, the accurate speed measurement of the solid metal wheels with smooth surfaces of freight wagons. In this paper, a contactless, eddy-current-based speed sensor is proposed for applications where the speed of a smooth conductive surface is to be measured; but contact to or modification of this target surface is prohibited. The proposed speed sensor is comprised of a permanent magnet (PM) rotor that is free to rotate above the target surface. The relative motion of the surface with respect to the PM field induces eddy currents in the surface, which leads to a torque being applied on the rotor. Consequently, the PM rotor speeds up until it reaches a steady rotational speed that is proportional to the speed of the target surface. Three models are proposed. They are a 2D finite-element model, a 2D analytical model, and a 3D combined numerical/ analytical model. Measurements are taken on multiple hardware prototypes to validate the analysis. Finally, a multi-objective (PM volume vs. dynamic performance) Pareto optimization is conducted for the proposed speed sensing system. The results show that smaller rotors with lower pole pair numbers generally have better dynamic performance as well as lower costs.**

***Index Terms*—Contactless speed sensor, eddy-current, optimization, permanent magnet.**

I. Introduction

Speed sensing is an essential feature in a broad range of closed-loop control systems found in transportation [1], automotive [2], machining and robotics [3]. In the operation of freight trains, an accurate measurement of the actual wheel speed is very important to the control of the train. Fig. 1 (a) shows a typical look of the train wheel. As can be seen, the wheels are made of solid metals with a smooth circumferential surface.

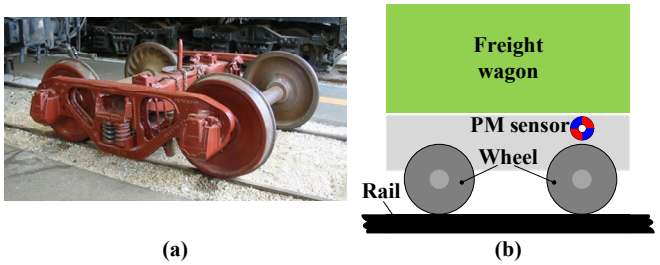

Fig. 1(a)Typical wheel appereance (b)Proposed speed sensing method

Traditional methods of speed sensing use optical or electromagnetic properties of the moving body, whose speed is to be measured. For instance, optical speed sensors utilize a code disk or an optical mark that is attached to the moving target body [4, 5]. However, because the freight trains normally run in harsh environments, such an optical modification of the wheel is not favorable for a robust and accurate measurement of the wheel speed.

Speed sensors that use magnetic properties may be applied in such harsh environments, such as Hall sensors or variable reluctance sensors. For example, a novel absolute magnetic rotary sensor is proposed [3] to measure the angular position of motors and robot joints. A rotary Hall effect sensor with an eccentrically mounted ring magnet is proposed to achieve a high measurement accuracy [6]. Another rotary magnetic position sensor with sinusoidally magnetized permanent magnet is proposed using Hall elements. An improved PMSM rotor position sensor is proposed based on linear Hall sensors [7]. As for variable reluctance sensors, an instantaneous rotation speed measurement systems is proposed for torsional vibration monitoring in [8]. A detailed modelling of an axial-flux variable reluctance resolver is proposed based on magnetic equivalent circuits and Schwarz-Christoffel Mapping in [9]. Another novel variable reluctance resolver for HEV/EV applications is proposed in [10]. A new noncontact displacement sensor employing a combination of variable reluctance technique and Hall effect sensing is designed and developed in [11]. However, these methods require a non-uniform magnetic property to be detected, which is the spatial variance of the magnetic permeance for variable reluctance sensors; and the magnetic field distribution for Hall sensors. For measuring the speed of the freight train wheel with smooth surfaces, these methods are also not suitable.

An interesting contactless speed sensing method is described in [12]. It uses a U-shaped inductor to place a series of magnetic marks on a moving steel surface. The surface's speed is then estimated based on the time difference between those marks being picked up by magnetic field sensors placed at different locations along the direction of motion. Obviously, this method cannot be applied to measure the speed of non-magnetic metals such as aluminum. A contactless speed sensor that uses eddy currents in conductive materials is discussed in [13]. The sensor is comprised of three co-planar coils placed above the target surface. An AC current is injected into the center coil, which induces eddy currents in the target surface. The motion of the target surface changes the eddy current distribution, which

leads to a voltage difference in the side coils that is proportional to the speed. The benefit of this method is that it does not need any inhomogeneity in optics or magnetics, and it can be applied to any conductive target, regardless it being magnetic or non-magnetic, as long as it is electrically conductive. However, a power supply is required not only to operate the measurement electronics, but also to inject the required current into the center coil and to supply the power dissipated in the target surface due to the eddy current losses.

In this paper, a new contactless eddy-current-based speed sensor is proposed as shown Fig. 1 (b). The motivation comes from the industrial need of measuring the speed of the solid metal wheel with smooth surfaces of freight wagons in harsh environments. The sensor includes a permanent magnet (PM) rotor that is free to rotate around its axis. When placed near the target surface (wheel), the relative motion of the target surface and the PM field induces eddy currents in the target surface, leading to a torque being applied on the PM rotor. Consequently, the PM rotor speeds up until it reaches a rotational speed proportional to the speed of the target surface. The proposed contactless speed sensor can be used to measure the surface speed of both translating and rotating smooth surfaces without needing any modification thereof, provided that the target surface is electrically conductive. Moreover, it has additional benefits such as a low-cost and simple construction (no need of additional equipment for signal injection or making magnetic marks), suitable to work in harsh environments (not affected by dust or light), and self-powering potential [14, 15]. Table I gives a comparison of different speed sensing methods in the literature.

TABLE I
COMPARISON OF DIFFERENT SPEED SENSING METHODS IN THE LITERATURE

	Target surface special requirement?	Suitable for harsh environments?	Possible to self-power?	Complexity	Cost
Optical sensor	Need modification	No	No	Simple	High
Hall sensor	Must be magnetic or salient surface	Yes	No	Simple	High
Variable reluctance sensor	Must be salient surface	Yes	No	Simple	High
U-shaped magnetic marks [12]	Must be magnetic surface	Yes	No	Complex	High
Current injection [13]	Any conductive surface	Yes	No	Complex	High
This paper	Any conductive surface	Yes	Yes	Simple	Low

The rest of the paper is arranged as follows: The principle of operation of the proposed speed sensor is detailed in Section II. In Section III, three different models are discussed, namely a two-dimensional finite-element model (2D FEM), a 2D analytical and a three-dimensional (3D) numerical/analytical combined model. An experimental analysis is carried out in Section IV. A good agreement between the models and measurements validates the models. In Section V, a multi-objective (PM volume vs. dynamic performance) Pareto optimization is conducted for the proposed speed sensor.

II. PRINCIPLE OF OPERATION

Fig. 2 shows the basic setup of the proposed speed sensor. A wheel comprising radially magnetized, alternating-pole PMs mounted on a ferromagnetic shaft, henceforth called the PM rotor, is free to rotate around its axis. It is placed above a moving, conductive target body whose speed is to be measured, which is henceforth referred to as the target surface. When the target surface is in motion as shown in Fig. 2, the magnetic field generated by the PM rotor induces eddy currents in the target surface. Thus, through this eddy-current coupling, a torque applies on the PM rotor and the PM rotor starts to rotate. The rotor then speeds up until it reaches a steady state speed. In other words, the working principle is very similar to the eddy-current coupler discussed in [16-20], or to the energy harvester described in [21-25].

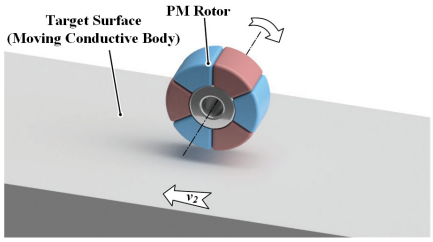

Fig. 2. General description of the proposed speed sensor.

For the PM rotor, a synchronous rotational speed ω_0 can be defined as

$$\omega_0 = \frac{v_2}{r_1 + g} \tag{1}$$

where v_2 is the speed of the target surface, r_1 is the radius of the PM rotor and g is the air gap length [21]. This allows the definition of the slip s as follows

$$s = \frac{\omega_1 - \omega_0}{\omega_1} \tag{2}$$

where ω_1 is the rotational speed of the PM rotor. This is similar to the well-known slip definition in induction machines, where $s < 0$ represents a generative operation mode. Ideally, $s = 0$ would mean idling, meaning there is no relative motion between PM field and the target surface, no eddy currents induced in the target surface, and consequently no torque acting on the PM rotor and no losses in the target surface. Nevertheless, the non-constant air gap caused by the round shape of the PM rotor results in the no-torque slip to deviate from $s = 0$ [21].

The steady state value of ω_1 depends on several factors such as the size of the rotor (width, inner and outer radii), the number of pole pairs, the remanent flux density of the magnets, and the air gap length as well as the electrical conductivity and magnetic permeability of the target surface. However, when the speed sensor application is considered, all the above-mentioned parameters except for the target surface speed are fixed by design, and a one-to-one correspondence exists between the PM

rotor and the target surface speeds. Consequently, the target speed can be measured by observing the speed of the PM rotor, which is very practical using a variety of methods such as Hall sensors, or pick-up coils [13]. In practice, bearing friction from the PM rotor acts as an external load, and changes the steady-state value of ω_1. Moreover, an additional load may also be present if, for example, the wheel is also being used as an energy harvester (as discussed in [14, 21]) to power its own signal electronics to form a self-powering speed sensor. Even though such external loads change the steady-state speed of the PM rotor, it will still depend on the target surface speed. Therefore, the relationship between these two speeds will be analyzed in detail in the following sections.

III. Modeling

Three different modeling methods are used in this work: 2D FEM, 2D analytical and 3D combined FEM/analytical. The two 2D models have a good agreement with the measurements, particularly for prototypes featuring a low bearing friction (about 0.1 mNm). However, when the bearing friction (or additional external load) becomes larger (about 10 mNm), the 2D models approach their limits because the 3D edge effect becomes more prominent compared to the low-friction region. All three modeling approaches are detailed in the following.

A. 2D Finite Element Model

Fig. 3 shows the magnetic field and eddy current distribution for a three-pole-pair speed sensor, calculated by a commercially available and commonly used 2D FEM software [26]. As is denoted by the white arrows in the figure, the six magnets are magnetized in the radial direction, with the red ones magnetized inwards and the blue ones magnetized outwards. An iron core is also modeled, which is surrounded by the PMs. The true motions of the PM rotor (rotation around its center axis) and the target surface (translation along the horizontal axis) are both modeled using moving meshes. Symmetric boundary conditions are applied on the horizontal ends of the model domain for simulating an infinitely long target surface. A time-transient solver is used to observe the dynamic behavior of the system from standstill [27].

As seen from Fig. 3, the field distribution of a rotor with such segmentally magnetized PMs generates a similar pattern with a Halbach rotor [28]. The difference is that in an ideal Halbach rotor there is no magnetic field inside the rotor, which is not the case here.

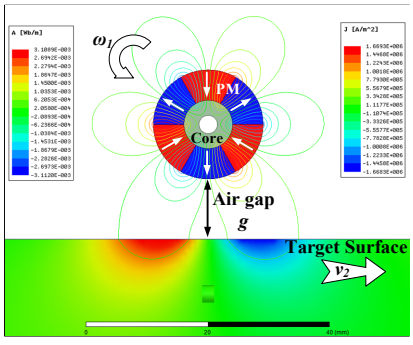

Fig. 3. Field and eddy current distribution of the 2D FEM.

B. 2D Analytical Model

From Fig. 3, it could be observed that the PM rotor comprising discrete PMs and a magnetic core/shaft can be approximated by an idealized Halbach rotor for simplitcity, although the PMs are not arranged in the Halbach array, because the higher order harmonics of the field can be neglected especially at large air gaps. The explicit model of the B field of such an iron-cored rotor can be expressed in polar coordinates as shown in [29]. Then the eddy currents in the target surface can be calculated by Ampere's law, from which the torque and the speed of PM rotor can also be calculated [30-33]. The general formulas for the 2D B field are listed in the Appendix.

C. 3D Numerical/Analytical Combined Model

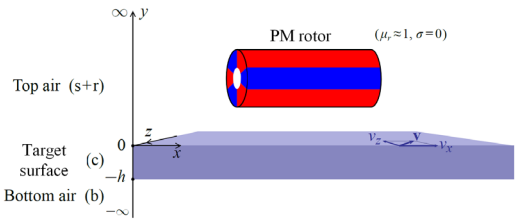

Fig. 4. Problem geometry for the 3D model: A vertically layered material setup with infinite horizontal extension (x, z) is assumed.

The geometry assumed for the 3D model is displayed in Fig. 4. The B field of the PM rotor surrounded by nothing but air is calculated by a 3D magnetostatic FEM simulation. To emulate the time-dependence of the field, FEM results are needed for various rotor angles θ. To keep the calculation effort to a minimum, instead of actually modifying and re-running the magnetostatic model, the field data from a single simulation at θ=0 is evaluated at different tilted planes as shown in Fig. 5. Doing so, the 3D FEM model is only simulated once for every single geometry of the PM rotor.

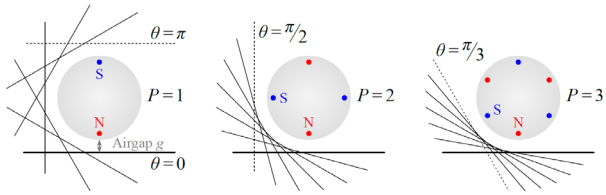

Fig. 5. Location of the FEM data capture planes, depending on the number of pole pairs P.

A mathematically concise overview of this method is presented in the Appendix. The treatment is kept short since this paper focuses mainly on the experimental verification and optimization of the proposed speed sensor. A more detailed derivation of the model will be published in subsequent works.

The advantage of the 3D model is that it combines the accuracy of a full 3D numerical model and the fast speed of an analytical model. On one side, the magnetic field of a rotor can be modelled as accurately as possible, taking the actual shape and magnetization pattern of the PMs into consideration, especially the 3D edge effect. Moreover, the static magnetic

field of a certain rotor needs to be simulated only once, based on which the performance of the speed sensor can be calculated for any air gap, target surface conductivity and permeability, as well as any speed of the target surface. This significantly reduces simulation time compared to a full 3D transient FEM model, which needs to be re-run for any modification of those parameters.

IV. Experimental Analysis

In order to verify the proposed models, five prototypes were built and tested. Fig. 6 and Table II show a picture of the test setup and define its key parameters. A 5.5 kW, 1950 rpm, inverter-fed induction machine is used to rotate a large aluminum wheel, which is the target surface whose surface speed is to be measured. An encoder at the drive machine's shaft provides an accurate reference rotational speed of the target surface. An adjustable positioning table is used for mounting the PM rotor prototypes (one at a time,) and setting the air gap accurately. The prototypes are positioned on the same level with the center of the aluminum wheel and are horizontally away from the right side surface of the aluminum wheel with a certain air gap. The curvature of the aluminum wheel may cause some increase of the air gap at the edge of the speed sensor. Since the diameter of the aluminum wheel is 450 mm, which is 10 times larger than the size of the prototypes, the target surface can still be assumed as a "flat" surface. Fig. 7 depicts the five PM rotor prototypes and Table III summarizes the key parameters thereof.

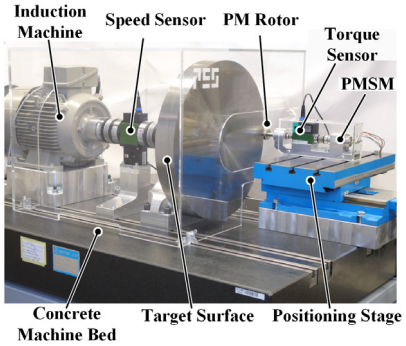

Fig. 6. Test setup.

TABLE II
KEY PARAMETERS OF THE TEST SETUP

Parameter	Symbol	Value
PM rotor core material		Construction steel
Radius of target surface wheel	r_2	225 mm
Depth of target surface wheel	h_1	45 mm
Target surface material		Al: EN AW-6082 (Ac-112)
Target surface conductivity	κ_2	24…32 MS/m
Target surface permeability	μ_2	$\mu 0$

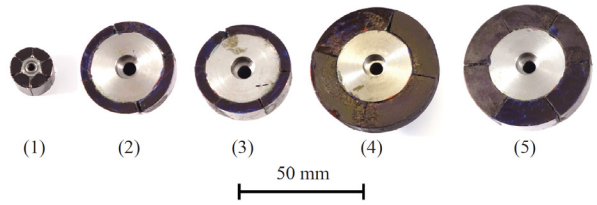

Fig. 7. Five prototypes.

TABLE III
PROTOTYPE PARAMETERS

No.	D_o (mm)	D_i (mm)	Width (mm)	Pole Pair	B_{rem} (T)	Magnetization direction
1	18	8	12	3	1.2	Parallel
2	36	28	10	2	1.0	Radial
3	36	28	10	3	1.0	Radial
4	50	30	10	2	1.25	Parallel
5	50	30	10	3	1.2	Parallel

In the typical speed sensing applications, the total friction torque will be limited to only the bearing friction, which is expected to be in the range of about 0.1 mNm for practical sizes and speeds. However, there may be cases where the sensor is loaded with a higher torque, for example by an increased friction due to operation in harsh environment, or due to the double-purpose use of the speed sensor also as an energy harvester [21] powering its own signal electronics.

For this reason, two modes of operations are studied in this section: low-friction mode and high-friction mode. The low-friction operation mode is studied using prototype No. 1, where typical low-friction bearings are used without any additional load. A coil is used around the prototype to measure the speed of the rotor by measuring the induced voltage, as shown in Fig. 8 (a). The results show a good agreement between all three proposed models and measurements.

On the other hand, the high-friction operation mode is studied using the other four prototypes having much larger size, by loading the PM rotor with additional high-friction bearings. In order to comprehensively study the robustness of the sensor in high-friction conditions, the torque-speed characteristics of the proposed speed sensing system is also studied. A torque sensor is connected to the rotor as shown in Fig. 8 (b). The prototypes are mounted with a shaft that is connected to a torque sensor through a pair of high-friction bearings and a small coupler. Then the torque sensor is connected through a big coupler to a small PMSM whose speed can be measured accurately and be adjusted by a three-phase variable resistive load. All the additional high-friction bearings contribute to the total friction to mimic the high-friction operation. The test results show a better performance of the 3D model than the 2D FEM and analytical model at high-friction conditions. Both steady state and dynamic characteristics are tested and analyzed.

A. Steady State Analysis

1) Low-friction operation mode

Prototype No. 1 is tested under a low bearing friction condition. The friction of the rotor is measured by accelerating the rotor to high speeds, letting it freewheel, and then measuring the speed profile. The deceleration and the corresponding friction torque can be derived with the knowledge of the inertia, which is called a "rundown" test. The measurements show a very low value of bearing friction, which is about 0.05 to 0.15 mNm. An average of 0.10 mNm can be selected considering such low values. This low bearing friction case is a typical case of a speed sensor because generally no load would be applied to the rotor. Fig. 9 shows the results of

the measurement and the proposed models at different air gaps of 2, 4, 6 and 8 mm. As the figure displays, the measurement shows a good linearity and all the proposed models match the measurements very well. The 3D model has the best agreement for all the air gaps. The 2D analytical model has almost equally good agreement with the 3D model at small air gaps of 2, 4 and 6 mm, while at 8 mm air gap it shows a little deviation from the measured results. The 2D FEM has almost equally good agreement with the 3D model at 8 mm air gap, while it shows some discrepancies at smaller air gaps.

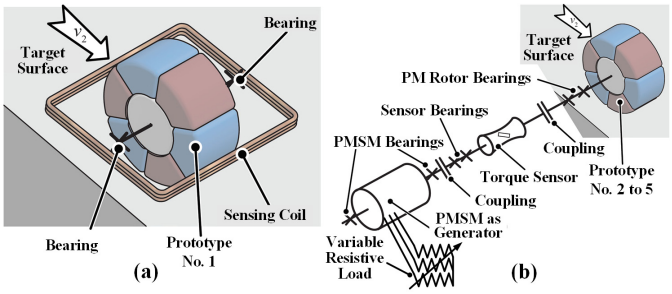

Fig. 8. (a) Low-friction mode setup. (b) High-friction mode setup.

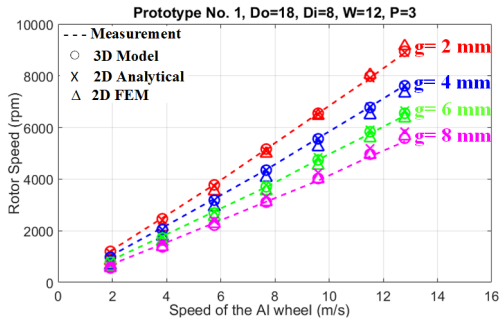

Fig. 9. Comparison of the measurement results and the proposed models.

2) *High-friction operation mode*

The overall friction of the setup shown in Fig. 8(b) is measured with a rundown test, which is shown in Fig. 10. It includes the friction of all the high-friction bearings. A linear fit of the measurement results in:

$$T_{friction} = -1.401\times10^{-6}\times\omega_m(rpm) - 0.004 \qquad (3)$$

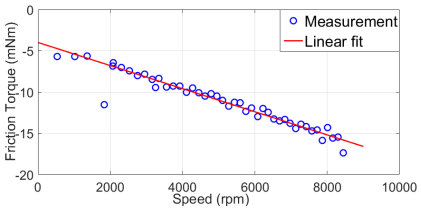

Fig. 10. Derived friction torque agaist rotor speed.

From Fig. 10, we can see that the friction torque ranges from about 5 mNm to 15 mNm and shows a good linearity with the speed. This new friction torque is about 100 times larger than typical values. After the friction is measured, the proposed model can be verified by comparing the torque speed curve predicted by the 3D model against the measurement results. A variable resistor is connected as the load to the small PMSM that is connected to the PM rotor in order to get different torques at different speed values. Fig. 11 and Fig. 12 show the torque speed curves of prototypes No. 3 and No. 5 at different air gaps at different target surface speeds. The data shows the model and the measurement match well. There is a little discrepancy of prototype No. 5 at 10 mm air gap. This is because the curvature of the target surface becomes more significant at larger air gaps than at smaller ones. Note that the shape of the torque speed curve is very similar to an induction machine because both of the rotors are activated by the slip speed and the eddy current and torque induced consequently.

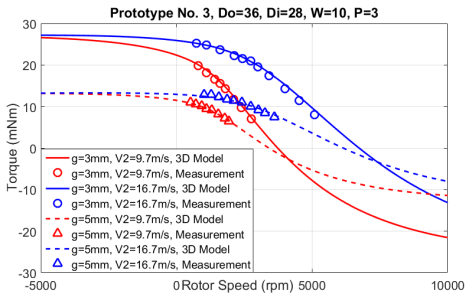

Fig. 11. Comparison of the measurement and the 3D model of prototype No. 3.

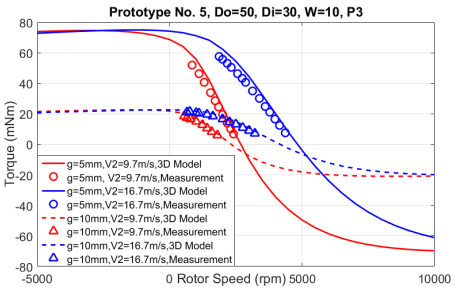

Fig. 12. Comparison of the measurement and the 3D model of prototype No. 5.

Fig. 13 and Fig. 14 show the comparison of the measured steady state speed of the No. 2 and No. 5 prototypes against the 3D model at different air gaps of 2, 4, 6 and 8 mm. From the figure we can see that the 3D model gives a very good prediction of the steady state speed at different air gaps.

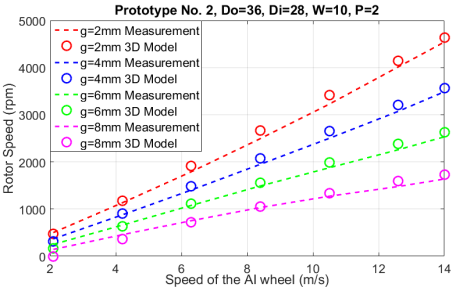

Fig. 13. Comparison of the measured steady state speed and the 3D model of prototype No. 2.

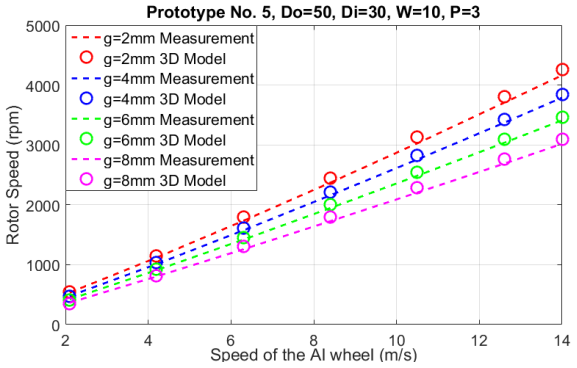

Fig. 14. Comparison of the measured steady state speed and the 3D model of prototype No. 5.

Fig. 15 shows the comparison of all three proposed models against measurements of prototype No. 4 at 4 mm and 8 mm air gaps. It can be seen that the 2D models (FEM and analytical) do not match as well as the 3D model against measurements. The larger the air gap, the greater the difference between the 2D models and the measurements is.

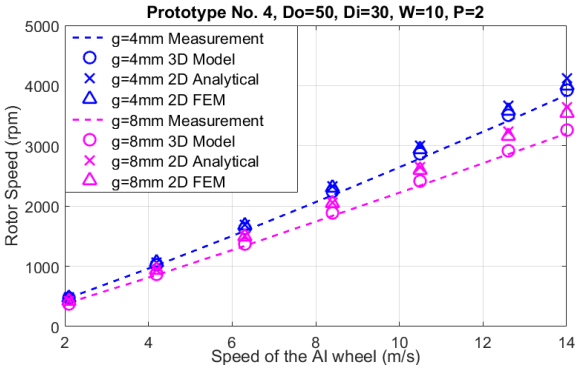

Fig. 15. Comparison of different models vs measurement of prototype No.4.

The reason behind this mismatch of the 2D models at high friction is interesting to analyze. Due to the assumption of an infinite wide rotor in the 2D models, the 3D edge effect is neglected. The edge effect results in a leakage or fringing flux at the edge of the rotor, which decreases the magnetic coupling and the resultant torque. Fig. 16 shows the comparison of the torque speed curve of prototype No. 4 between the 3D model and the 2D analytical model at 8 mm air gap. The solid curves are the results from the 2D analytical model, while the dash curves are from the 3D model. It can be seen that the 3D model has a much lower torque than the 2D analytical model. The two green and red straight lines represent the high and low friction, respectively. The different colors stand for different target surface speeds from 2.1 to 14 m/s. For example, it can be easily seen that at low friction the cross points (steady state speed) of the red line (low friction) and two blue lines (solid and dash for v_2=14 m/s) almost overlap with each other (blue triangular marks). When at high friction, the two cross points (blue circular marks) have a much larger distance due to the inaccurately larger torque predicted by the 2D analytical model. The larger the friction, the less accurate the 2D models will be.

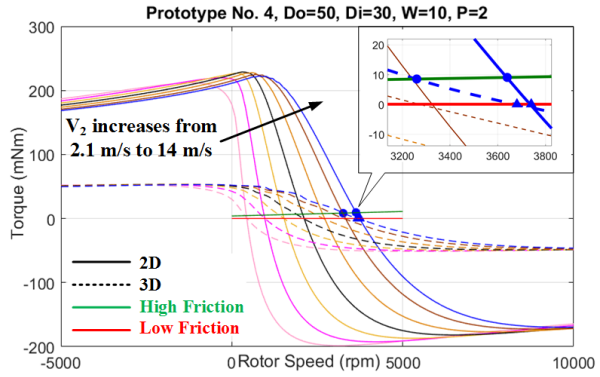

Fig. 16. Comparison of the torque speed curve of prototype No. 4 between the 3D model and the 2D analytical model at 8 mm air gap.

B. Transient Analysis

The proposed speed sensing system uses the eddy-current coupling to transfer the speed information of the target surface to another non-contacting physically rotating body whose speed can be detected easily. For an accurate transient response, the rotor has to have a good dynamic performance, for example, the rotor speed has to stick as closely to the target speed as possible. This dynamic performance depends on many parameters such as size, thickness of the magnets, pole-pair number, and air gap.

Fig. 17, Fig. 18 and Fig. 19 show the transient response comparison of prototypes 1, 3 and 5 between the measurement results and the proposed 3D model under different air gaps. It can been seen that under low-friction conditions (Fig. 17) the proposed 3D model has a very good agreement with the measurement results. The 2D analytical model has almost the same results as the 3D model although it is not shown here. In large-friction region (Fig. 18 and Fig. 19), the 3D model has a little discrepancy of the steady state speed against the measurement, which is already shown in the steady state analysis. However, it still gives a good estimation of the dynamic performance of the prototypes.

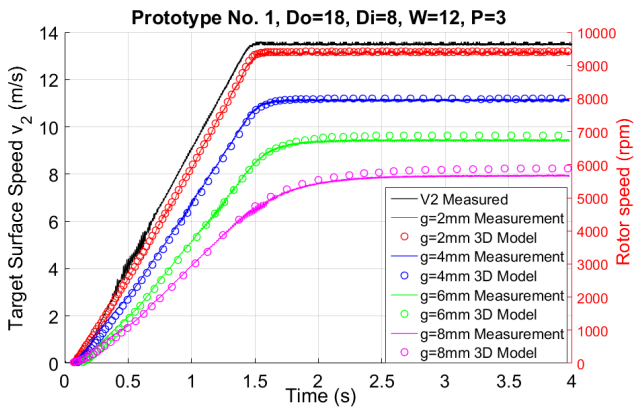

Fig. 17. Comparison of the transient response of prototype No. 1 between measurement and the 3D model.

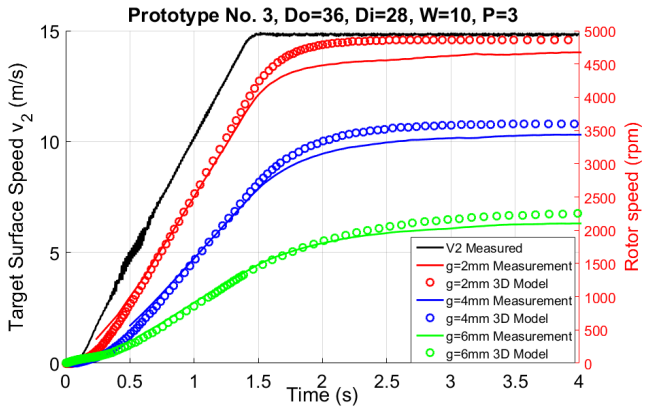

Fig. 18. Comparison of the transient response of prototype No. 3 between measurement and the 3D model.

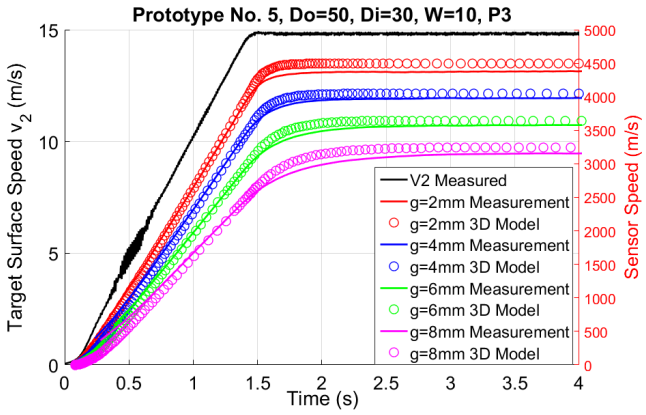

Fig. 19. Comparison of the transient response of prototype No. 5 between measurement and the 3D model.

By comparing these three figures it can easily be seen that prototype No. 1 has a much better dynamic performance than prototype No. 3, while the prototype No. 5 is somewhere between them. For example, at 2 mm air gap (red) the prototype No. 1 follows the speed of the aluminum wheel (target surface) very fast and accurately. When the target surface speed goes into steady state (at 1.5s), the rotor also gets into steady state almost simultaneously. However, at the same air gap prototype No. 3 goes into steady state about one second (or more) after the steady state of the aluminum wheel. The reason is the larger friction and the larger inertia for prototype No. 3. However, even under the same high friction, prototype No. 5 has a faster response than prototype No. 3 due to the larger size even though larger size means larger inertia. The drawback is that it costs more for larger volume of the PMs. For the same prototype, the smaller the air gap, the better dynamic performance the system has due to the better magnetic coupling and the larger resultant torque.

From the aforementioned observation, it can be seen that there is an engineering trade-off between the PM volume (cost) and dynamic performance (response speed) of the proposed speed sensing system. In the next section a Pareto optimization will be conducted based on the proposed model.

V. Optimization

In order to evaluate the dynamic performance of the speed sensor, a rising time t_r is defined as the response time of the PM rotor from standstill to 90% of the steady state speed under a step excitation of 10 m/s of the target surface. The smaller the t_r, the faster the PM rotor will respond to the change of the target surface speed, which is very important for a good speed sensor. The simulation time is set to be at maximum 10 seconds, which means if the rising time is longer than 10 seconds, it will be clamped to 10 seconds.

TABLE IV
Parameters Simulated for Optimization

v_2 (m/s)	g (mm)	P	r_o (mm) Small to large	d (mm) Light to dark
10	10	1(●),2(♦), 3(▲),4(■)	10, 15, 20, 25, 30	1, 2, 3, 4, 5

Fig. 20 shows the Vol_{mag}-t_r Pareto optimization [34, 35] of the PM rotor at the typical low bearing friction at a 10 mm air gap. The x axis is the rising time t_r and the y axis is the volume of the magnets in mm^3. The closer the optimal design to the origin is, the better. Table IV shows the parameters simulated in the optimization. Three key parameters, namely the PM outer radius (r_o), the PM thickness ($d = r_o - r_i$) and the pole pair number (P) are chosen to be the degree of freedom. r_o varies from 10 mm to 30 mm with a step of 5 mm, which is denoted by the different size of the marks from small to large in the figure. d varies from 1 to 5 mm with a step of 1 mm, which is represented by the darkness of the marks. The darker the mark, the thicker the PM is. Different shapes with different colors stand for different pole pair numbers as follows: of 1 (red circles ●), 2 (green diamonds ♦), 3 (blue triangles ▲) and 4 (yellow squares ■). More pole pair numbers are not considered because of the assembly difficulty. Fig. 20 (1) to (4) are the cases of 1, 2, 3 and 4 pole pairs, respectively. Fig. 20 (5) to (7) are the comparisons between two different pole pair numbers of 1&2, 2&3 and 3&4, respectively. Fig. 20 (8) is the overall optimization of all the simulated cases with iron shaft rotors. Fig. 20 (9) is the rotors with aluminum shaft. From the figure the following can be observed:

1. From Fig. 20 (1) to (4), there is an obvious Pareto front for all the cases. For 1, 2, and 3 pole-pair rotors the trend is that under the same thickness, smaller rotors have better dynamic performance and lower magnet volume. However, for 4 pole-pair rotors it is not necessarily the case. For 1 mm thick PMs, the rotors have to be over a certain out diameter in order to have a quick response.

2. From Fig. 20 (5) to (7), we can observe that for the same thickness and size, 2 pole-pair rotors generally have better dynamic performance than the other pole pair numbers, because the green diamonds ♦ are generally shifted to the left side of the red circles ● (Fig. 20 (5)) and the blue triangles ▲ (Fig. 20 (6)), which are on the left side of the yellow squares ■ (Fig. 20 (7)). However, for some cases of extreme sizes (smallest rotors in Fig. 20 (5) and largest rotors in Fig. 20 (6),) the opposite is observed.

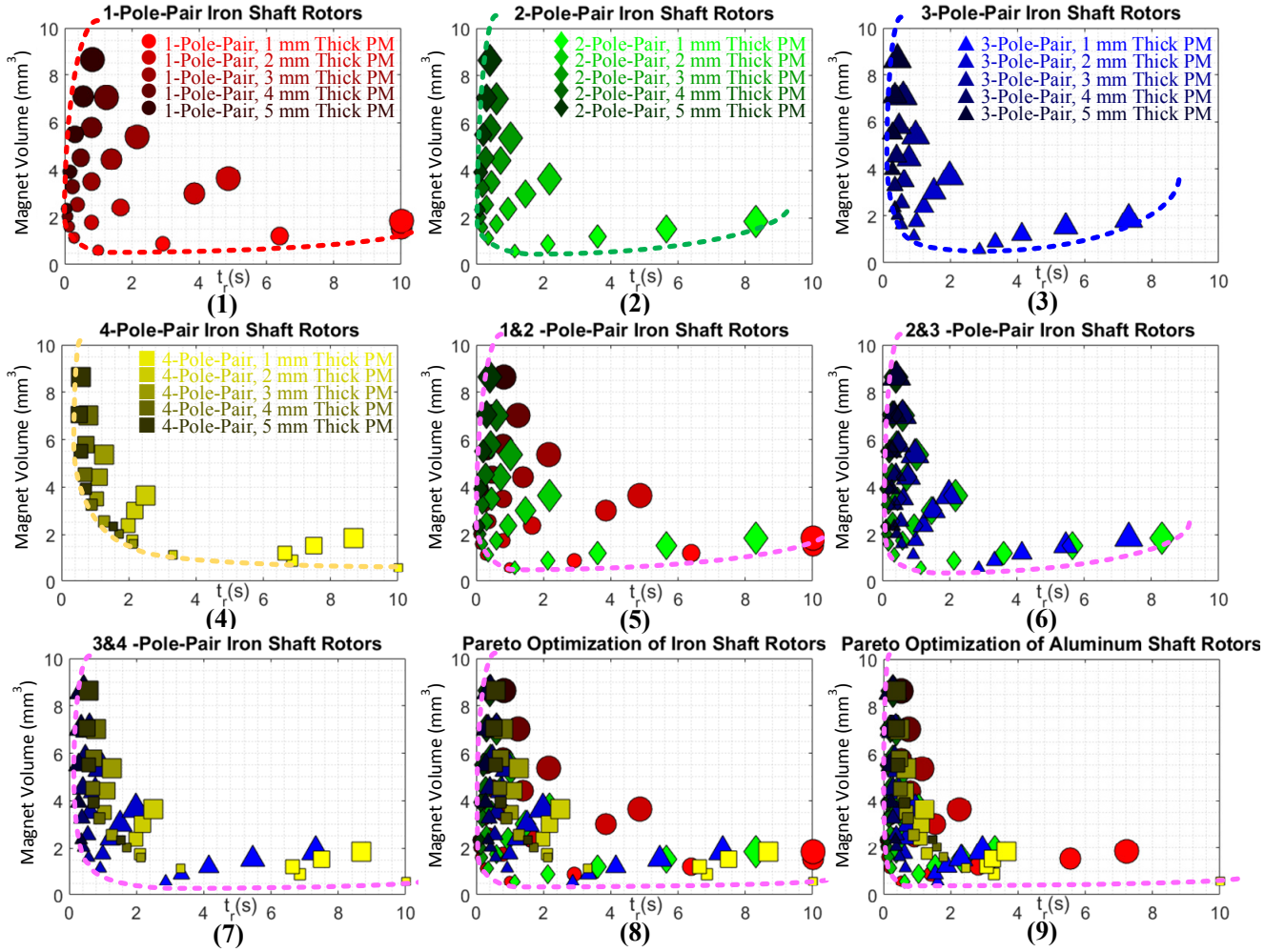

Fig. 20. Pareto optimization of different rotors. Different sizes of the marks represent different r_o from 10 mm to 30 mm with a step of 5 mm. Different darknesses represent different thichness of the PMs. The darder the mark is, the thicker the PMs are. Different shapes with different colors stand for different pole pair number of 1 (red circles ●), 2 (green diamonds ♦) 3 (blue triangles ▲) and 4 (yellow squares ■).

3. The thickness of the magnets has a much greater impact on the larger rotors than smaller ones in terms of dynamic performance. For instance, for 30 mm outer radius samples (largest marks), if we increase the thickness of the PMs from 1 mm to 2 mm, the rising time drops significantly for each pole pair number, but for smaller rotors this improvement is not that significant.

4. From Fig. 20 (8), it can be observed that for the special case of 10 mm air gap, a thickness of 3 mm is enough for almost all combinations, which have a rising time less than 3 seconds. This implies that an investment in the PM thickness for over 3 mm is not worth its value in this case.

In conclusion, three candidates are considered to be the optimal designs. They all have 1 pole pair with an outer diameter of 10 mm. The one with the best dynamic performance would be of 5 mm thickness. It has a t_r of 0.06s, but the Vol_{mag} is 2.36 mm^3. The one with the best economic benefit has 1 mm thickness. It only has a Vol_{mag} of 0.60 mm^3. However, the rising time would be longer, which is 0.99 s. A more balanced candidate is the 2 mm thick one, which has a t_r of 0.28s and a Vol_{mag} of 1.13 mm^3. All their 2 pole-pair counterparts have a similar performance with a little increase in the rising time (shown in parentheses). So, it can be concluded that, for this special case of 10 mm air gap under low bearing friction, smaller rotors with lower pole pair numbers generally perform better in both dynamics and costs, among which the thicker the PMs are, the faster the response speed is, which also costs more. Table V gives a conclusion of the best candidates.

TABLE V
BEST CANDIDATE PARAMETERS

Parameter	Symbol	Fastest	Cheapest	Balanced
Rising time (s)	t_r	0.06 (0.11)	0.99 (1.14)	0.28 (0.36)
PM volume (mm^3)	Vol_{mag}	2.36	0.60	1.13
Pole pair No.	P	1 (2)	1 (2)	1 (2)
PM outer radius (mm)	r_o	10	10	10
PM thickness (mm)	d	5	1	2

The poor dynamic performance of rotors with thin and large-radius magnets is due to the fact that the useless part of the inertia (iron shaft) is too large. For example the inertia of the magnets of the 30 mm radius, 1 mm thickness rotor is 1.3e-5 kg·m^2, while the inertia of the iron shaft is 8.7e-5 kg·m^2, which is about 6.7 times greater. So rotors with shafts made from much lighter material than iron (for example, aluminum shafts) should

have a better dynamic performance. Although the magnetic field will be attenuated due to the use of non-magnetic shaft, because of the Halbach pattern of the rotor magnets, the outside magnetic field will not decrease much. The magnetic field generated by the PM rotor with an aluminum shaft can be modified in the model according to [29]:

Fig. 20 (9) shows the Pareto optimization of the speed sensors with aluminum shafts. As can be seen, all the samples have reduced their rising time, compared to their iron shaft counterparts, especially for those rotors with large and thin PMs. The majority of the samples have a rising time less than 4 seconds. The basic observations and the optimal designs are the same as in the iron-shaft case.

VI. Conclusion

In this paper, a contactless eddy-current-based rotational speed sensor is proposed for measuring the speed of a smooth conductive surface where modification/touching of the target is undesired, for example, in the application of measuring the speed of freight wagon wheels. Three different models of 2D FEM, 2D analytical and 3D model are proposed to analyze the system. When under low-friction/no load conditions, all three of the models have a good agreement with the measurement results. When under large-friction/load conditions, the 3D model still shows a good agreement with the measurement results, which is better than the 2D models because of the 3D edge effect. Torque speed curve comparisons are given for the validation of the proposed models. Finally, based on the proposed models, a PM volume/response speed Pareto optimization is conducted for the proposed speed sensing system. The results show that smaller rotors with lower pole pair numbers generally have a better dynamic performance as well as lower costs. Future study will be focused on the analysis and implementation of a self-powering speed sensing system using the energy harvesting features described in [25].

VII. Appendix

The 2D magnetic flux density (B) field of the rotating PM rotor is simplified as an idealized Halbach rotor as in [36] using the following equations [29]:

$$B_r(r,\theta;t)=\frac{C_{xia}}{r^{P+1}}\cdot\cos(P\theta-\omega_e t)$$
$$B_\theta(r,\theta;t)=\frac{C_{xia}}{r^{P+1}}\cdot\sin(P\theta-\omega_e t) \quad (4)$$

$$\omega_e = P\cdot\omega_m \quad (5)$$

where B_r and B_θ are the flux density component in the radial and circumferential directions, respectively; P is the pole pair number of the PM rotor; ω_m and ω_e are the mechanical and electrical frequency, respectively; C_{xia} is a defined coefficient and can be calculated by (6) for iron shaft and by (7) for aluminum shaft:

$$C_{xia}=B_{rem}\cdot\left(\frac{2P}{P+1}\right)\frac{r_0^{2P}(r_0^{P+1}-r_i^{P+1})}{(1+\mu_r)r_0^{2P}-(1-\mu_r)r_i^{2P}} \quad (6)$$

$$C_{xia}=B_{rem}\cdot\left(\frac{2P}{P+1}\right)\frac{(1+\mu_r)r_0^{2P}(r_0^{P+1}-r_i^{P+1})}{(1+\mu_r)^2 r_0^{2P}-(1-\mu_r)^2 r_i^{2P}} \quad (7)$$

where B_{rem} is the remanence flux density of the PM; μ_r is its relative permeability; r_o and r_i are the outer and inner radii of the PM rotor.

These two formulas can be transformed to Cartesian coordinates as follows:

$$B_{sx}=\frac{C_{xia}}{(x+iy)^{P+1}}$$
$$B_{sy}=\frac{i\cdot C_{xia}}{(x+iy)^{P+1}} \quad (8)$$

For the 3D model, the general solution in the conductive region can be derived as follows:

$$\beta=\sqrt{\xi^2+\zeta^2+i\mu\sigma(\omega+\xi v_x+\zeta v_z)}$$
$$\mathcal{B}_{cx}=C_{cx}e^{\beta y}+D_{cx}e^{-\beta y}$$
$$\mathcal{B}_{cy}=C_{cy}e^{\beta y}+D_{cy}e^{-\beta y} \quad (9)$$
$$\mathcal{B}_{cz}=C_{cz}e^{\beta y}+D_{cz}e^{-\beta y}$$

where μ and σ are the permeability and conductivity of the conductive region, respectively.

In the nonconductive regions, the field is:

$$\alpha=\sqrt{\xi^2+\zeta^2}$$
$$\mathcal{B}_{nx}=i\xi C_n e^{\alpha y}+i\xi D_n e^{-\alpha y}$$
$$\mathcal{B}_{ny}=\alpha C_n e^{\alpha y}-\alpha D_n e^{-\alpha y} \quad (10)$$
$$\mathcal{B}_{nz}=i\zeta C_n e^{\alpha y}+i\zeta D_n e^{-\alpha y}$$

where the subscript c and n represent conductive and nonconductive region, respectively; $\mathcal{B}(\xi, y, \zeta)$ is the Fourier transform of the magnetic field $B(x,y,z)$ and is defined as follows:

$$B(x,y,z)=\frac{1}{(2\pi)^2}\int_{-\infty}^{\infty}\int_{-\infty}^{\infty}\mathcal{B}(\xi,y,\zeta)e^{i\xi x}e^{i\zeta z}d\xi d\zeta \quad (11)$$

The decay factors β and α and all amplitude coefficients C and D are functions of the spatial Fourier frequencies ξ, ζ and can be expressed as follows:

$$denom=(\beta+\alpha\mu_{rc})^2-e^{-2\beta h}(\beta-\alpha\mu_{rc})^2$$
$$Bcomb=i\xi\mathcal{B}_{sx}-\alpha\mathcal{B}_{sy}+i\zeta\mathcal{B}_{sz}$$
$$C_{cz}=\beta(\beta+\alpha\mu_{rc})\cdot\frac{\mu_{rc}(\alpha\mathcal{B}_{sz}+i\xi\mathcal{B}_{sy})}{\alpha\cdot denom}$$
$$D_r=\frac{\mathcal{B}_{sy}}{\alpha}+\{(\beta+\alpha\mu_{rc})+\ldots e^{-2\beta h}(\beta-\alpha\mu_{rc})\}\cdot\frac{\mu_{rc}Bcomb}{\alpha\cdot denom}$$
$$D_{cx}e^{\beta h}=-\beta(\beta-\alpha\mu_{rc})\cdot\frac{\mu_{rc}(\alpha\mathcal{B}_{sx}+i\xi\mathcal{B}_{sy})}{\alpha\cdot denom}e^{-\beta h}$$
$$D_{cy}e^{\beta h}=-(\beta-\alpha\mu_{rc})\cdot\frac{\mu_{rc}Bcomb}{denom}e^{-\beta h} \quad (12)$$
$$C_{cx}=\beta(\beta+\alpha\mu_{rc})\cdot\frac{\mu_{rc}(\alpha\mathcal{B}_{sx}+i\xi\mathcal{B}_{sy})}{\alpha\cdot denom}$$
$$D_{cz}e^{\beta h}=-\beta(\beta-\alpha\mu_{rc})\cdot\frac{\mu_{rc}(\alpha\mathcal{B}_{sz}+i\zeta\mathcal{B}_{sy})}{\alpha\cdot denom}e^{-\beta h}$$
$$C_{cy}=-\beta(\beta+\alpha\mu_{rc})\cdot\frac{\mu_{rc}Bcomb}{denom}$$
$$C_b e^{-ah}=-2\beta\frac{\mu_{rc}Bcomb}{\alpha\cdot denom}e^{-\beta h}$$

At the region interface planes, the usual boundary conditions apply, i. e. continuity of normal B_y and tangential H_x, H_z. Special attention is required for the top air region, as it contains a superposition of the incident field B_s (given by the magnetostatic FEM solution) and a reflected field B_r, i. e. the change in field caused by the presence of the moving conductive plate:

$$B_{top}=B_s+B_r \quad (13)$$

The eddy currents in the target surface can be calculated by Ampere's law as follows:

$$J_{cx}=C_{Jx}e^{\beta y}+D_{Jx}e^{-\beta y}$$
$$J_{cy}=0 \quad (14)$$
$$J_{cz}=C_{Jz}e^{\beta y}+D_{Jz}e^{-\beta y}$$

where J is the current density and the coefficients are derived as follows:

$$BsumX = i\xi i\zeta\alpha\mathcal{B}_{sx} + i\zeta(\beta^2-\alpha^2)B_{sy} + \alpha(\beta^2-\zeta^2)\mathcal{B}_{sz}$$
$$BsumZ = i\xi i\zeta\alpha\mathcal{B}_{sz} + i\xi(\beta^2-\alpha^2)B_{sy} + \alpha(\beta^2-\xi^2)\mathcal{B}_{sx}$$
$$C_{Jx} = (\beta+\alpha\mu_{rc})BsumX\cdot\frac{1}{\mu_0\alpha\cdot denom} \quad D_{Jx}e^{\beta h} = (\beta-\alpha\mu_{rc})BsumX\cdot\frac{e^{-\beta h}}{\mu_0\alpha\cdot denom} \tag{15}$$
$$C_{Jz} = -(\beta+\alpha\mu_{rc})BsumZ\cdot\frac{1}{\mu_0\alpha\cdot denom} \quad D_{Jz}e^{\beta h} = -(\beta-\alpha\mu_{rc})BsumZ\cdot\frac{e^{-\beta h}}{\mu_0\alpha\cdot denom}$$

With all the field known, the average torque can be calculated as follows:

$$M_{z,avg} = \mathrm{Re}\{-\frac{1}{4\mu_0}\sum_{n=1,3,5,\ldots}^{H}\sum_{x,z}(x\cdot\left|B_{y[n]}\right|^2 - x\cdot\left|B_{x[n]}\right|^2 - x\cdot\left|B_{z[n]}\right|^2)\Delta x\Delta z - \ldots$$
$$\frac{\hat{y}_0}{2\mu_0}\sum_{n=1,3,5,\ldots}^{H}\sum_{x,z}B_{x[n]}B_{y[n]}\Delta x\Delta z\} \tag{16}$$

REFERENCES

[1] C. Gong, S. Zhang, F. Zhang, J. Jiang, and X. Wang, "An integrated energy-efficient operation methodology for metro systems based on a real case of Shanghai metro line one," *Energies,* vol. 7, pp. 7305-7329, 2014.

[2] 30 E. Systems. Speed Sensors Application Note [Online]. Available: https://www.mclaren.com/appliedtechnologies/products/download_support_document/?id=10

[3] Z. Zhang, F. Ni, Y. Dong, C. Guo, M. Jin, and H. Liu, "A novel absolute magnetic rotary sensor," *IEEE Transactions on Industrial Electronics,* vol. 62, pp. 4408-4419, 2015.

[4] C. Gong, T. Habetler, J. Restrepo, and B. Soderholm, "Direct position control for ultra-high speed switched reluctance machines based on non-contact optical sensors," in *2017 IEEE International Electric Machines and Drives Conference (IEMDC)*, 2017, pp. 1-6.

[5] C. Gong, S. Li, T. Habetler, J. A. Restrepo, and B. Soderholm, "Direct Position Control for Ultrahigh-Speed Switched-Reluctance Machines Based on Low-Cost Nonintrusive Reflective Sensors," *IEEE Trans. Ind. Appl.,* vol. 55, pp. 480-489, 2019.

[6] S.-T. Wu, J.-Y. Chen, and S.-H. Wu, "A rotary encoder with an eccentrically mounted ring magnet," *IEEE Transactions on Instrumentation and Measurement,* vol. 63, pp. 1907-1915, 2014.

[7] J. Hu, J. Zou, F. Xu, Y. Li, and Y. Fu, "An improved PMSM rotor position sensor based on linear Hall sensors," *IEEE Transactions on Magnetics,* vol. 48, pp. 3591-3594, 2012.

[8] T. Addabbo, M. Di Marco, A. Fort, E. Landi, M. Mugnaini, V. Vignoli, *et al.*, "Instantaneous Rotation Speed Measurement System Based on Variable Reluctance Sensors for Torsional Vibration Monitoring," *IEEE Transactions on Instrumentation and Measurement,* 2018.

[9] H. Saneie, Z. Nasiri-Gheidari, and F. Tootoonchian, "Design-oriented modelling of axial-flux variable-reluctance resolver based on magnetic equivalent circuits and Schwarz–Christoffel mapping," *IEEE Transactions on Industrial Electronics,* vol. 65, pp. 4322-4330, 2018.

[10] X. Ge, Z. Zhu, R. Ren, and J. Chen, "A novel variable reluctance resolver for HEV/EV applications," *IEEE Transactions on Industry Applications,* vol. 52, pp. 2872-2880, 2016.

[11] K. Sandra, B. George, and V. J. Kumar, "Combined variable reluctance-Hall effect displacement sensor," *IEEE Transactions on Instrumentation and Measurement,* vol. 67, pp. 1169-1177, 2018.

[12] J. Lopera, M. Prieto, F. Linera, G. Vecino, and J. A. González, "A new speed measurement system," *IEEE Ind. Appl. Magz.,* vol. 11, pp. 44-51, 2005.

[13] A. Tüysüz, M. Flankl, J. W. Kolar, and A. Mütze, "Eddy-current-based contactless speed sensing of conductive surfaces," in *IEEE Annual Southern Power Electronics Conference (SPEC)*, 2016, pp. 1-6.

[14] M. Flankl, A. Tüysüz, C. Gong, T. Stolz, and J. W. Kolar, "Analysis and Modeling of Eddy-Current Couplings for Auxiliary Power Generation on a Freight Train Wagon," *IEEE Power and Energy Technology Systems Journal,* vol. 5, pp. 139-147, 2018.

[15] Magnic Light [Online]. Available: http://www.magniclight.com

[16] T. Lubin and A. Rezzoug, "Steady-state and transient performance of axial-field eddy-current coupling," *IEEE Trans. Ind. Electron.,* vol. 62, pp. 2287-2296, 2015.

[17] Z. Mouton and M. J. Kamper, "Modeling and optimal design of an eddy current coupling for slip-synchronous permanent magnet wind generators," *IEEE Trans. Ind. Electron.,* vol. 61, pp. 3367-3376, 2014.

[18] J. Wang and J. Zhu, "A Simple Method for Performance Prediction of Permanent Magnet Eddy Current Couplings Using a New Magnetic Equivalent Circuit Model," *IEEE Trans. Ind. Electron.,* vol. 65, pp. 2487-2495, 2018.

[19] S. Mohammadi, M. Mirsalim, S. Vaez-Zadeh, and H. A. Talebi, "Analytical modeling and analysis of axial-flux interior permanent-magnet couplers," *IEEE Trans. Ind. Electron.,* vol. 61, pp. 5940-5947, 2014.

[20] A. S. Erasmus and M. J. Kamper, "Computationally Efficient Analysis of Double PM-Rotor Radial-Flux Eddy Current Couplers," *IEEE Trans. Ind. Electron.,* vol. 53, pp. 3519-3527, 2017.

[21] M. Flankl, A. Tüysüz, and J. W. Kolar, "Analysis of a watt-range contactless electromechanical energy harvester facing a moving conductive surface," in *2015 IEEE Energy Conversion Congress and Exposition (ECCE)*, 2015, pp. 414-420.

[22] M. Flankl, A. Tüysüz, and J. W. Kolar, "Cogging Torque Shape Optimization of an Integrated Generator for Electromechanical Energy Harvesting," *IEEE Trans. Ind. Electron.,* vol. 64, pp. 9806-9814, 2017.

[23] M. Flankl, A. Tuysuz, L. de Oliveira Baumann, and J. Kolar, "Energy Harvesting with Single-Sided Linear Induction Machines featuring Secondary Conductive Coating," *IEEE Trans. Ind. Electron.,* 2018.

[24] D. Strothmann, "Device for contactless current generation, in particular bicycle dynamo, vehicle lighting system and bicycle," US Patent 9236761B2, 2013.

[25] M. Flankl, A. Tüysüz, I. Subotic, and J. W. Kolar, "Novel contactless axial-flux permanent-magnet electromechanical energy harvester," in *2016 IEEE Applied Power Electronics Conference and Exposition (APEC)*, 2016, pp. 623-630.

[26] ANSYS Maxwell [Online]. Available: https://www.ansys.com/products/electronics/ansys-maxwell

[27] R. Nasiri-Zarandi, M. Mirsalim, and A. Tenconi, "A novel hybrid hysteresis motor with combined radial and axial flux rotors," *IEEE Trans. Ind. Electron.,* vol. 63, pp. 1684-1693, 2016.

[28] N. Paudel and J. Z. Bird, "General 2-D steady-state force and power equations for a traveling time-varying magnetic source above a conductive plate," *IEEE Trans. Magn.,* vol. 48, pp. 95-100, 2012.

[29] Z. Xia, Z. Zhu, and D. Howe, "Analytical magnetic field analysis of Halbach magnetized permanent-magnet machines," *IEEE Trans. Magn.,* vol. 40, pp. 1864-1872, 2004.

[30] B. Prieto, M. Martínez-Iturralde, L. Fontán, and I. Elosegui, "Analytical calculation of the slot leakage inductance in fractional-slot concentrated-winding machines," *IEEE Trans. Ind. Electron.,* vol. 62, pp. 2742-2752, 2015.

[31] Y. Oner, Z. Zhu, L. Wu, X. Ge, H. Zhan, and J. Chen, "Analytical on-load subdomain field model of permanent-magnet Vernier machines," *IEEE Trans. Ind. Electron.,* vol. 63, pp. 4105-4117, 2016.

[32] Y. Liu, S. Niu, and W. Fu, "Design of an electrical continuously variable transmission based wind energy conversion system," *IEEE Trans. Ind. Electron.,* vol. 63, pp. 6745-6755, 2016.

[33] L. Sun, M. Cheng, H. Wen, and L. Song, "Motion control and performance evaluation of a magnetic-geared dual-rotor motor in hybrid powertrain," *IEEE Trans. Ind. Electron.,* vol. 64, pp. 1863-1872, 2017.

[34] Q. Wang, S. Niu, and L. Yang, "Design optimization and comparative study of novel dual-PM excited machines," *IEEE Trans. Ind. Electron.,* vol. 64, pp. 9924-9933, 2017.

[35] G. Bramerdorfer, J. A. Tapia, J. Pyrhonen, and A. Cavagnino, "Modern Electrical Machine Design Optimization: Techniques, Trends, and Best Practices," *IEEE Trans. Ind. Electron.,* 2018.

[36] S. Paul and J. Bird, "Improved analytic model for eddy current force considering edge-effect of a conductive plate," in *2016 International Conference on Electrical Machines (ICEM)*, 2016, pp. 789-795.

Cheng Gong (S'16) received his B.S. degree in electrical engineering from Shanghai Jiao Tong University, Shanghai, China, in 2012 and Ph.D. degree from Georgia Institute of Technology, Atlanta, GA, USA in 2019. In summer 2017, he was invited as a visiting scholar in the Power Electronic Systems Lab, ETH-Zurich, Switzerland. In summer 2018, he worked as an R&D intern with ANSYS/Maxwell group in Canonsburg, PA, USA. He is

currently working as a R&D motor design engineer at Whirlpool Cooperation, Benton Harbor, MI, USA. His research interests include the design, optimization and control of various kinds of electric machines including PM machines, reluctance machines, axial flux machines for both high-speed and low-speed applications.

Arda Tüysüz (S'10–M'13) received his B.Sc. degree in electrical engineering from Istanbul Technical University. Istanbul, Turkey, in 2006; his M.Sc. degree in electrical power engineering from RWTH Aachen University, Aachen, Germany, in 2009; and his Ph.D. degree in electrical drives from the Swiss Federal Institute of Technology (ETH) Zurich, Zurich, Switzerland, in 2015. Between 2015 and 2017, he worked as a Post-Doctoral Researcher with the Power Electronic Systerns Laboratory of ETH Zurich. He is currently a research scientist with the ABB Corporate Research Center in Ladenburg, Germany. His research interests include novel electrical machine topologies, self-sensing control of high-speed electrical machines and wide-bandgap power devices for very efficient and compact electrical drive systems.

Michael Flankl (S'12) received the B.Sc. degree in mechatronics from JKU Linz, Austria, in 2012, the Ph.D. degree from Swiss Federal Institute of Technology (ETH) Zurich in 2019. From 2010 to 2012, he was a freelancer at the Electrical Engineering/Electronics Department, Engineering Center Steyr GmbH (a branch of Magna Powertrain), St. Valentin, Austria. His research interests and professional experience include special electric machines, drives, railway and automotive transportation systems, and optimization and control thereof.

Tibor Stolz received the degree in electrical engineering from the Swiss Federal Institute of Technology (ETH) Zurich, Zürich, Switzerland, with a focus on power electronics, electric drives, and renewable energy. In his master's thesis, he developed analytical eddy-current models for various applications in mechatronics, including a graphical user interface for easy access to the simulations. Since 2017, he has been with the Power Electronic Systems Laboratory, ETH Zurich, extending this project as a Scientific Assistant.

Johann W. Kolar (M'89–SM'04–F'10) received the Ph.D. degree (summa cum laude) in electrical engineering from the Vienna University of Technology, Austria. He is currently a Full Professor and the Head of the Power Electronic Systems Laboratory, Swiss Federal Institute of Technology (ETH) Zurich. He has proposed numerous novel PWM converter topologies and modulation and control concepts and has supervised over 60 Ph.D. students. He has published over 750 scientific papers in international journals and conference proceedings and three book chapters. He has filed more than 150 patents. He has presented over 20 educational seminars at leading international conferences. The focus of his current research is on ultra-compact and ultra-efficient SiC and GaN converter systems, wireless power transfer, solid-state transformers, power supplies on chip, and ultra-high speed and ultra-lightweight drives, bearingless motors, and energy harvesting. He has received the 25 IEEE Transactions and Conference Prize Paper Awards, the 2014 IEEE Power Electronics Society R. David Middlebrook Achievement Award, the 2016 IEEE William E. Newell Power Electronics Award, the 2016 IEEE PEMC Council Award, and two ETH Zurich Golden Owl Awards for excellence in teaching. He has initiated and/or is the founder of four ETH spin-off companies. He has served as the IEEE PELS Distinguished Lecturer from 2012 to 2016.

Thomas Habetler (S'82-M'83-SM'92-F'02) received the B.S.E.E. degree in 1981 and the M.S. degree in 1984, both in electrical engineering, from Marquette University, Milwaukee, WI, and the Ph.D. degree from the University of Wisconsin-Madison, in 1989. From 1983-1985 he was employed by the Electro-Motive Division of General Motors as a Project Engineer. Since 1989, he has been with the Georgia Institute of Technology, Atlanta, USA, where he is currently a Professor of Electrical and Computer Engineering. His research interests are in protection and condition monitoring of electric machines and building electrical systems, power electronics and drives. He has published over 300 technical papers in the field. He is a regular consultant to industry in the field of condition-based diagnostics for electrical systems. Dr. Habetler received the 2012 IEEE-PELS Harry A. Owen Distinguished Service Award, and the 2012 Gerald B. Kliman Innovator Award from IAS. He was the inaugural recipient of the IEEE-PELS "Diagnostics Achievement Award," and a recipient of the EPE-PEMC "Outstanding Achievement Award." He has also received a number of IEEE-IAS prize paper awards. He has served on the IEEE Board of Directors as the Division II Director, and on the Technical Activities Board, the Member and Geographic Activities Board, the IEEE-USA Board of Directors, and is a past president of the Power Electronics Society. In addition, Dr. Habetler has served in numerous chair and committee positions at the corporate level of the IEEE. Dr. Habetler is a Fellow of the IEEE, with the citation, "for contributions to electric motor control and condition monitoring."